# LTP Modeling and Analysis of Frequency Coupling in PLL-Synchronized Converters for Harmonic Power Flow Studies

Federico Cecati, *Member, IEEE*, Johanna Kristin Maria Becker, *Student Member, IEEE*, Sante Pugliese, *Member, IEEE* Yihui Zuo, *Member, IEEE*, Marco Liserre, *Fellow, IEEE*, Mario Paolone, *Fellow, IEEE*

***Abstract*—As known, nonlinear loads in power systems originate harmonic distortion and power quality issues. Converter-interfaced loads exhibit a nonlinear behaviour as well and may largely contribute to increase the harmonic pollution. The nonlinearities introduced by the PLL-synchronization and power control originate, indeed, a coupling mechanism between fundamental and harmonic frequencies. These harmonic coupling effects are not captured by traditional Norton/Thevenin equivalent converter models, leading to inaccurate harmonic power flow analyses. This paper proposes a Linear Time Periodic model of a PLL-synchronized converter to be used in Harmonic Power Flow analyses. A realistic 18-bus distribution grid hosting substantial amount of power-electronic interfaced resources is used as a case study. It is revealed that, in high grid loadability condition and with distorted grid supply voltage, the harmonics are significantly amplified by the converters and the fundamental components of the buses voltages are reduced, representing a risk for the voltage stability. This phenomenon is also influenced by the tuning of the current control loop and the PLL. The accuracy of the presented analyses is validated by comparing the harmonic power flow results with time-domain simulations.**

***Index Terms*—Harmonic Power Flow, Voltage Source Converter, Phase-Locked Loop, Distribution Grid, Microgrid**

## NOMENCLATURE

### Grid nomenclature

- $\mathcal{R}$ The set of nodes with grid following converters and loads, with cardinality $|\mathcal{R}|$.
- $\mathcal{S}$ The set of nodes with slack buses and grid forming converters, with cardinality $|\mathcal{S}|$.
- $h$ Harmonic order.
- $H_{max}$ Maximum harmonic order considered in the analyses.
- $k_l$ Grid loadability factor.

### Modeling nomenclature

- $\Delta\theta \in \mathbb{R}$ Harmonic disturbance on the PLL tracked angle.
- $\hat{\mathbf{A}}_\kappa \in \mathbb{C}^{[4(2H_{max}+1)]\times[4(2H_{max}+1)]}$ The system Toepliz matrix for the control software.
- $\hat{\mathbf{B}}_\kappa \in \mathbb{C}^{[4(2H_{max}+1)]\times[4(2H_{max}+1)]}$ The input Toepliz matrix for the control software.
- $\hat{\mathbf{C}}_\kappa \in \mathbb{C}^{[2(2H_{max}+1)]\times[4(2H_{max}+1)]}$ The output Toepliz matrix for the control software.
- $\hat{\mathbf{D}}_\kappa \in \mathbb{C}^{[2(2H_{max}+1)]\times[4(2H_{max}+1)]}$ The feedthrough Toepliz matrix for the control software.
- $\hat{\mathbf{E}}_\kappa \in \mathbb{C}^{[4(2H_{max}+1)]\times[2(2H_{max}+1)]}$ The disturbance input Toepliz matrix for the control software.
- $\hat{\mathbf{F}}_\kappa \in \mathbb{C}^{[2(2H_{max}+1)]\times[2(2H_{max}+1)]}$ The disturbance feedthrough Toepliz matrix for the control software.
- $\hat{\mathbf{H}}_{\mathcal{R}\times\mathcal{R}} \in \mathbb{C}^{[3|\mathcal{R}|(2H_{max}+1)]\times[3|\mathcal{R}|(2H_{max}+1)]}$ The block of $\hat{\mathbf{H}}$ linking $\hat{\mathbf{V}}_{\gamma,\mathcal{R}}$ and $\hat{\mathbf{I}}_{\varphi,\mathcal{R}}$.
- $\hat{\mathbf{H}}_{\mathcal{R}\times\mathcal{S}} \in \mathbb{C}^{[3|\mathcal{R}|(2H_{max}+1)]\times[3|\mathcal{S}|(2H_{max}+1)]}$ The block of $\hat{\mathbf{H}}$ linking $\hat{\mathbf{I}}_{\varphi,\mathcal{R}}$ and $\hat{\mathbf{I}}_{\varphi,\mathcal{S}}$.
- $\hat{\mathbf{H}}_{\mathcal{S}\times\mathcal{R}} \in \mathbb{C}^{[3|\mathcal{S}|(2H_{max}+1)]\times[3|\mathcal{R}|(2H_{max}+1)]}$ The block of $\hat{\mathbf{H}}$ linking $\hat{\mathbf{V}}_{\gamma,\mathcal{S}}$ and $\hat{\mathbf{V}}_{\gamma,\mathcal{R}}$.
- $\hat{\mathbf{H}}_{\mathcal{S}\times\mathcal{S}} \in \mathbb{C}^{[3|\mathcal{S}|(2H_{max}+1)]\times[3|\mathcal{S}|(2H_{max}+1)]}$ The block of $\hat{\mathbf{H}}$ linking $\hat{\mathbf{V}}_{\gamma,\mathcal{S}}$ and $\hat{\mathbf{I}}_{\varphi,\mathcal{S}}$.
- $\hat{\mathbf{Y}} \in \mathbb{C}^{[3(2H_{max}+1)]\times[3(2H_{max}+1)]}$ Converter harmonic frequency coupling matrix.
- $\widetilde{\theta} \in \mathbb{R}$ PLL tracked angle for the fundamental frequency.
- $A_\kappa(t) \in \mathbb{R}^{4\times4}$ The system matrix for the control software LTP model.
- $B_\kappa(t) \in \mathbb{R}^{4\times4}$ The input matrix for the control software LTP model.
- $C_\kappa(t) \in \mathbb{R}^{2\times4}$ The output matrix for the control software LTP model.
- $D_\kappa(t) \in \mathbb{R}^{2\times4}$ The feedthrough matrix for the control software LTP model.
- $E_\kappa(t) \in \mathbb{R}^{4\times2}$ The disturbance input matrix for the control software LTP model.
- $F_\kappa(t) \in \mathbb{R}^{2\times2}$ The disturbance feedthrough matrix for the control software LTP model.
- $i_{\varphi,\kappa} \in \mathbb{R}^2$ Converter output current expressed in $dq$ frame
- $i_{\varphi,\pi} \in \mathbb{R}^3$ Converter output current expressed in $abc$ frame
- $i^*_\varphi \in \mathbb{R}^2$ Current loop reference current expressed in $dq$ frame
- $P^* \in \mathbb{R}$ Active power reference from the system-level controller.
- $Q^* \in \mathbb{R}$ Reactive power reference from the system-level controller.
- $u_\kappa \in \mathbb{R}^4$ Input for the control software model.
- $v_{\alpha,\kappa} \in \mathbb{R}^2$ Converter voltage reference expressed in $dq$ frame
- $v_{\alpha,\pi} \in \mathbb{R}^3$ Converter voltage reference expressed in $abc$ frame
- $v_{\gamma,\kappa} \in \mathbb{R}^2$ Converter output voltage expressed in $dq$ frame
- $v_{\gamma,\pi} \in \mathbb{R}^3$ Converter output voltage expressed in $abc$ frame
- $w^*_\kappa \in \mathbb{R}^2$ Reference for the converter from the system-level controller.
- $y_\pi \in \mathbb{R}^6$ Output for the power hardware model.

## I. Introduction

POWER electronics converters are becoming one of the main assets in modern distribution networks. Indeed, they operate as smart interfaces for renewable energy sources, DC loads (e.g. electric vehicle charging stations) or battery energy storage systems (BESS) [1], [2]. However, researches and field experiences confirmed that the massive presence of power converters can increase the harmonic pollution, especially in power distribution grids [3], [4]. Several papers investigated the mechanism of harmonic generation and amplification in this context, nevertheless still many aspects of the phenomenon remain not entirely understood [2], [3], [5].

As known, the converters nonlinearities play a fundamental role in its harmonic response. While conventional nonlinear loads generate harmonics due to nonlinear *physical* elements (e.g. diodes, electronic ballast) [6], converter-interfaced loads present nonlinearities in their low-level *control* [7]. Several studies analyzed through linear models the influence of the converter control system on the harmonic generation and propagation into the grid, and investigated the possible presence and excitation of harmonic resonances emerging from improper control tuning [2], [8]–[10]. Linear converter models, e.g. impedance-based Norton/Thevenin models [11]–[13] or Linear Time Invariant (LTI) state-space models [14], can identify the attenuation/amplification and phase shift introduced by the converter at each harmonic frequency [2]. Nevertheless, these models cannot capture the effect of the converter nonlinearities responsible of the cross-coupling among different harmonic orders (*frequency coupling terms*), which can distort the input waveform and even generate new harmonics, similarly to other kinds of nonlinear loads [6], [8], [9]. Because of the frequency coupling phenomena, the voltage/current harmonics in the power system can affect also the fundamental voltages/currents and vice versa, modifying the electrical power flow in the network with a possible impact on the voltage stability [15]–[17]. Frequency coupling phenomena in voltage source converters (VSCs) have been studied in literature for the analysis of harmonics interactions [18]–[20], small-signal stability [10], [21] and high-frequency resonances in modular multilevel converters (MMC) [22], [23] among them. Nevertheless, the impact of the frequency coupling terms on Harmonic Power Flow (HPF) analyses of distribution grids is nowadays still scarcely investigated in the literature.

The main VSC control nonlinearities, responsible of the frequency coupling phenomena, are the power control and the reference frame transformation, as shown in Fig. 1 [7], [24]. The power control, indicated as current reference calculation $\rho$ in Fig. 1, generates the current reference by dividing the power set-points by the direct-axis grid voltage $v_{\gamma_d}$. The angle $\widetilde{\theta}$ tracked by the PLL is used by the nonlinear reference frame transformations, and is furthermore affected by the grid harmonics [25]. Therefore, both the modeling of power control and the synchronization are important for harmonic studies.

Linear Time Periodic (LTP) models are valuable tools for the analysis of frequency coupling effects generated by nonlinearities [2], [10], [23], [26], [27]. Some researches proposed LTP converter models and transformed them into an equivalent

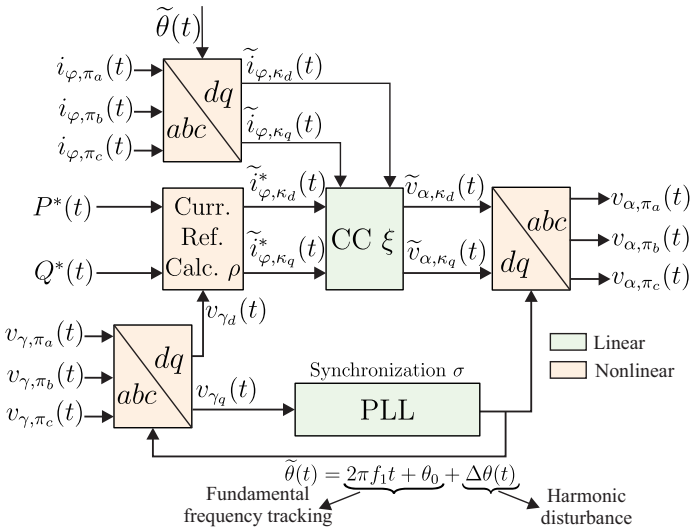


Fig. 1: The modeling of the converter control software with consideration of the PLL synchronization.

LTI system according to Floquet theory, in order to perform small-signal stability analyses under distorted grid conditions [26], [28]. Another application of LTP systems is to model the converters frequency coupling effects for static power system analyses, i.e. Harmonic Power Flow. In this context, a LTP-based modeling framework for converter-dominated grids, and a relevant HPF formulation that can be solved through Newton-Raphson algorithm, has been proposed and validated in [8], [9].

The aforementioned modeling framework is adopted in this paper to study the effect of the converter control nonlinearities on the power system harmonic propagation, equilibrium point and stability. A converter-dominated 18 bus Cigré benchmark network is built within the HPF modeling framework by using converters LTP models [29].

The main research objectives and main novelties of this paper can be summarized as follows:

- The modeling and analysis of the frequency coupling phenomena related to the converters PLL synchronization by means of LTP modeling.
- The effects of the harmonic pollution on the fundamental voltages at the grid buses, under different grid operating conditions.
- The harmonics amplification effects in grid-connected VSCs caused by the control system nonlinearities, depending on the grid operating conditions.
- The effects of the VSCs control tuning (i.e. the current controller and the PLL bandwidth) on the harmonic propagation, with consideration of frequency coupling phenomena.

The paper is structured as follows: section II explains the LTP system theory, section III derives the converter model, section IV presents the HPF results on a VSC-dominated distribution grid and section V presents the conclusions.

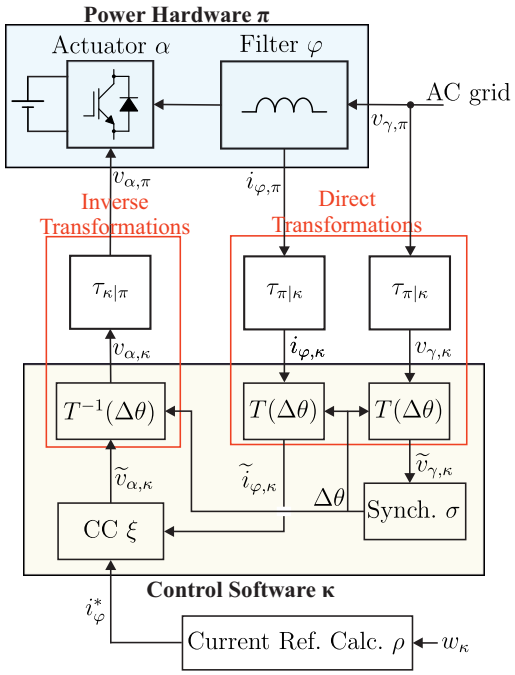


Fig. 2: The block diagram of the converter state-space model used for the HPF framework.

## II. Theoretical and Methodological Background

The proposed block scheme for the VSC modeling is depicted in Fig. 2. The power hardware $\pi$ is composed of a three-phase PWM actuator $\alpha$ represented by a two-level VSC and an L filter $\varphi$, modeled in the $abc$ coordinate frame. The dc-link voltage is assumed to be constant.

The converter control software $\kappa$ is realized in the $dq$ coordinate frame and includes the inner current control (CC) $\xi$, the PLL synchronization unit $\sigma$ and the rotation matrices $T(\Delta\theta)$, $T^{-1}(\Delta\theta)$ (see section III). The $abc/dq$ transformations, indicated with $\tau_{\pi|\kappa}$, $\tau_{\kappa|\pi}$, are used to interface power hardware and control software [8].

The current reference calculation block $\rho$ generates the current loop set-point $i^*_\varphi$ from the reference $w_\kappa$ coming from the power system-level controller.

The power hardware $\pi$ can be generically modeled as an LTP system in the $abc$ frame, as discussed in detail in [8]:

$$\begin{cases} \dot{x}_\pi(t) &= A_\pi(t)x_\pi(t) + B_\pi(t)v_{\alpha,\pi}(t) + E_\pi(t)v_{\gamma,\pi}(t) \\ y_\pi(t) &= C_\pi(t)x_\pi(t) + D_\pi(t)v_{\alpha,\pi}(t) + F_\pi(t)v_{\gamma,\pi}(t) \end{cases} \quad (1)$$

where $y_\pi = \begin{pmatrix} i_{\varphi,\pi} & v_{\gamma,\pi} \end{pmatrix}^T$. With the assumption of two-level topology for the actuator $\alpha$ operating in linear region, constant dc voltage and neglecting the switching effects, the model (1) becomes LTI (trivial case of LTP) [8], [23], [27].

The model of the control software block $\kappa$ in Fig. 2 is entirely defined in the $dq$ reference frame. Under undistorted and balanced grid conditions, being the control gains usually constant over time, the control software $\kappa$ can be considered Nonlinear Time Invariant (NLTI), in the form:

$$\begin{cases} \dot{x}_\kappa(t) &= f_\kappa(x_\kappa(t), u_\kappa(t), i^*_\varphi(t)) \\ v_{\alpha,\kappa}(t) &= h_\kappa(x_\kappa(t), u_\kappa(t), i^*_\varphi(t)) \end{cases} \quad (2)$$

where $x_\kappa = \begin{pmatrix} x_\xi & \Delta\theta & \Phi_\gamma \end{pmatrix}^T$, $x_\xi \in \mathbb{R}^2$ is the integral state of the current controller and $\Phi_\gamma \in \mathbb{R}$ is the integral state of the PLL. The input of the control software is defined as $u_\kappa = \begin{pmatrix} i_{\varphi,\kappa} & v_{\gamma,\kappa} \end{pmatrix}^T$. The nonlinearity of (2) is mainly due to the rotation matrices $T(\Delta\theta)$, $T^{-1}(\Delta\theta)$, and the investigation of its effect on the harmonic propagation is a primary objective in this paper and novelty with respect to [8], [9].

### A. Control software model time-periodicity in harmonic distorted conditions

In harmonic undistorted and balanced grid conditions, the $abc$ quantities $i_{\varphi,\pi}(t)$ and $v_{\gamma,\pi}(t)$ are purely sinusoidal in steady-state. The sinusoidal $abc$ quantities are transformed into *constant* $dq$ quantities $i_{\varphi,\kappa}(t)$ $v_{\gamma,\kappa}(t)$ by the reference frame transformations. The linearization of the control software $\kappa$ model (2) will be thus realized around a constant equilibrium point, denominated $\left(\bar{x}_\kappa, \bar{u}_\kappa, \bar{i}^*_\varphi\right)$, resulting in a LTI model [7], [8].

In the case of harmonic distorted conditions, the $abc$ quantities $i_{\varphi,\pi}(t)$ and $v_{\gamma,\pi}(t)$ are not purely sinusoidal; their transformation into the $dq$ frame results in not constant, rather *time periodic* signals $\left(\bar{x}_\kappa(t), \bar{u}_\kappa(t), \bar{i}^*_\varphi(t)\right)$.

The linearization of the model (2) is therefore realized in this case around steady-state time periodic operating trajectory:

$$\left(\bar{x}_\kappa(t), \bar{u}_\kappa(t), \bar{i}^*_\varphi(t)\right) = \left(\bar{x}_\kappa(t+T_1), \bar{u}_\kappa(t+T_1), \bar{i}^*_\varphi(t+T_1)\right) \quad (3)$$

assumed of period $T_1 = \frac{1}{f_1}$, with $f_1$ being the fundamental frequency of the system [7], [30].

The linearization, and in particular the *evaluation* of the control software model (2) around the time-periodic trajectory $\left(\bar{x}_\kappa(t), \bar{u}_\kappa(t), \bar{i}^*_\varphi(t)\right)$, makes it time periodic:

$$\begin{cases} \Delta\dot{x}_\kappa(t) &= A_\kappa(t)\Delta x_\kappa(t) + B(t)\Delta u_\kappa(t) + E(t)\Delta i^*_\varphi(t) \\ \Delta v_{\alpha,\kappa}(t) &= C_\kappa(t)\Delta x_\kappa(t) + D(t)\Delta u_\kappa(t) + F(t)\Delta i^*_\varphi(t) \end{cases} \quad (4)$$

with

$$\begin{cases} \Delta x_\kappa(t) &= x_\kappa(t) - \bar{x}_\kappa(t) \\ \Delta u_\kappa(t) &= u_\kappa(t) - \bar{u}_\kappa(t) \\ \Delta i^*_\varphi(t) &= i^*_\varphi(t) - \bar{i}^*_\varphi(t) \\ \Delta\dot{x}_\kappa(t) &= x_\kappa(t) - f_\kappa\left(\bar{x}_\kappa(t), \bar{u}_\kappa(t), \bar{i}^*_\varphi(t)\right) \\ \Delta v_{\alpha,\kappa}(t) &= v_{\alpha,\kappa}(t) - h_\kappa\left(\bar{x}_\kappa(t), \bar{u}_\kappa(t), \bar{i}^*_\varphi(t)\right) \end{cases} \quad (5)$$

and

$$\begin{cases} A_\kappa(t) &= \left.\dfrac{\partial f}{\partial x_\kappa}\right|_{x_\kappa=\bar{x}_\kappa(t),u_\kappa=\bar{u}_\kappa(t),i^*_\varphi=\bar{i}^*_\varphi(t)} \\ B_\kappa(t) &= \left.\dfrac{\partial f}{\partial u_\kappa}\right|_{x_\kappa=\bar{x}_\kappa(t),u_\kappa=\bar{u}_\kappa(t),i^*_\varphi=\bar{i}^*_\varphi(t)} \\ C_\kappa(t) &= \left.\dfrac{\partial h}{\partial x_\kappa}\right|_{x_\kappa=\bar{x}_\kappa(t),u_\kappa=\bar{u}_\kappa(t),i^*_\varphi=\bar{i}^*_\varphi(t)} \\ D_\kappa(t) &= \left.\dfrac{\partial h}{\partial u_\kappa}\right|_{x_\kappa=\bar{x}_\kappa(t),u_\kappa=\bar{u}_\kappa(t),i^*_\varphi=\bar{i}^*_\varphi(t)} \\ E_\kappa(t) &= \left.\dfrac{\partial f}{\partial i^*_\varphi}\right|_{x_\kappa=\bar{x}_\kappa(t),u_\kappa=\bar{u}_\kappa(t),i^*_\varphi=\bar{i}^*_\varphi(t)} \\ F_\kappa(t) &= \left.\dfrac{\partial h}{\partial i^*_\varphi}\right|_{x_\kappa=\bar{x}_\kappa(t),u_\kappa=\bar{u}_\kappa(t),i^*_\varphi=\bar{i}^*_\varphi(t)} \end{cases} \quad (6)$$

Regarding the Jacobian matrices in (6), $A_\kappa$ contains the state $x_\kappa(t)$ and the inputs $u_\kappa(t)$, $i^*_{\varphi,\kappa}(t)$, i.e. it is in the form $A_\kappa\left(x_\kappa(t), u_\kappa(t), i^*_{\varphi,\kappa}(t)\right)$ and the same yields for $B_\kappa$, $C_\kappa$, $D_\kappa$, $E_\kappa$, $F_\kappa$. The evaluation of the matrices in the form $\Gamma\left(x_\kappa(t), u_\kappa(t), i^*_\varphi(t)\right)$ around $\left(\bar{x}_\kappa(t), \bar{u}_\kappa(t), \bar{i}^*_\varphi(t)\right)$ according to (6) generates a LTP system with matrices in the form $\Gamma(t)$.

A challenge of using LTP models (as in (4)) for HPF studies is that the steady-state operating trajectory $\left(\bar{x}_\kappa(t), \bar{u}_\kappa(t), \bar{i}^*_\varphi(t)\right)$ of each VSC depends on the whole grid and is *unknown a priori* [7]. It becomes known only when the HPF analysis of the considered grid converges to its solution [8].

Therefore, the converters Jacobian matrices in (4) are required to have the form $\Gamma\left(x_\kappa(t), u_\kappa(t), i^*_\varphi(t)\right)$ in the HPF formulation, and the evaluation process (6) has to be redone at each Newton-Raphson iteration, updating $\left(\bar{x}_\kappa(t), \bar{u}_\kappa(t), \bar{i}^*_\varphi(t)\right)$ at each step according to the HPF solution of the previous iteration. This iterative evaluation of the LTP models allows both to consider the constant power behaviour of the VSCs and to correctly model the frequency coupling effects [7], [31].

Once the LTP model is obtained, the time-periodic vectors (5) and matrices (6) of the model (4) can be expressed with their Fourier series [8], with $x_\kappa(t)$ and $A_\kappa(t)$ in the form:

$$\begin{cases} x_\kappa(t) = \displaystyle\sum_{h=-H_{max}}^{H_{max}} X_{\mathbf{h}} \exp(jh2\pi f_1 t) \\ A_\kappa(t) = \displaystyle\sum_{h=-H_{max}}^{H_{max}} A_{\mathbf{h}} \exp(jh2\pi f_1 t) \end{cases} \quad (7)$$

where $X_{\mathbf{h}}$, $A_{\mathbf{h}}$ are respectively the complex Fourier coefficients of the periodic vector $x_\kappa(t)$ and matrix $A_\kappa(t)$. $h$ and $H_{max}$ are the generic and maximum harmonic order considered in the analysis, respectively. As known, LTI systems can be considered as particular cases of LTP systems where the Fourier coefficients $X_{\mathbf{h}}$, $A_{\mathbf{h}}$ are null for $h \neq 0$.

From the model (4), the static relationship between the Fourier coefficients of the states, inputs and outputs as in (7) can be derived and expressed through the harmonic-domain state-space model:

$$\begin{cases} j\Omega\hat{\mathbf{X}}_\kappa &= \hat{\mathbf{A}}_\kappa\hat{\mathbf{X}}_\kappa + \hat{\mathbf{B}}_\kappa\hat{\mathbf{U}}_\kappa + \hat{\mathbf{E}}_\kappa\hat{\mathbf{I}}^*_\varphi \\ \hat{\mathbf{V}}_{\alpha,\kappa} &= \hat{\mathbf{C}}_\kappa\hat{\mathbf{X}}_\kappa + \hat{\mathbf{D}}_\kappa\hat{\mathbf{U}}_\kappa + \hat{\mathbf{F}}_\kappa\hat{\mathbf{I}}^*_\varphi \end{cases} \quad (8)$$

by substituting the time-domain derivative operator with the frequency-domain operator $j\Omega$, defined as:

$$j\Omega = j2\pi f_1 \mathrm{diag}_{h\in[-H_{max},\dots H_{max}]}(h \cdot I) \quad (9)$$

and by using Toeplitz matrices constructed from the Fourier coefficients of the form $X_{\mathbf{h}}$, $A_{\mathbf{h}}$ as in (7), indicated with the hat notation, e.g. $\hat{\mathbf{X}}_\kappa$, $\hat{\mathbf{A}}_\kappa$ [8], [9]. The same procedure is applied to the power hardware model $\pi$ in (1), obtaining a model in the form:

$$\begin{cases} j\Omega\hat{\mathbf{X}}_\pi &= \hat{\mathbf{A}}_\pi\hat{\mathbf{X}}_\pi + \hat{\mathbf{B}}_\pi\hat{\mathbf{V}}_{\alpha,\pi} + \hat{\mathbf{E}}_\pi\hat{\mathbf{V}}_{\gamma,\pi} \\ \hat{\mathbf{Y}}_\pi &= \hat{\mathbf{C}}_\pi\hat{\mathbf{X}}_\kappa + \hat{\mathbf{D}}_\pi\hat{\mathbf{V}}_{\alpha,\pi} + \hat{\mathbf{F}}_\pi\hat{\mathbf{V}}_{\gamma,\pi} \end{cases} \quad (10)$$

### *B. Frequency coupling terms in PLL-synchronized VSCs*

For the interconnection of the harmonic state-space models of power hardware (10) and control software (8), the harmonic model of the transformations $\tau_{\pi|\kappa}$ and $\tau_{\kappa|\pi}$ in Fig. 2, denominated $\mathrm{T}_{\pi|\kappa}$ and $\mathrm{T}_{\kappa|\pi}$ respectively, must be derived (see section III).

After realizing the interconnections, a static frequency-domain LTP model of the VSC internal response from the VSC input voltage $v_{\gamma,\pi}$ (in harmonic domain $\hat{\mathbf{V}}_{\gamma,\pi}$) to the grid injected current $i_{\varphi,\pi}$ (in harmonic domain $\hat{\mathbf{I}}_{\varphi,\pi}$) is obtained:

$$\begin{cases} j\Omega\hat{\mathbf{X}}_{vsc} &= \hat{\mathbf{A}}_{vsc}\hat{\mathbf{X}}_{vsc} + \hat{\mathbf{E}}_{vsc}\hat{\mathbf{V}}_{\gamma,\pi} \\ \hat{\mathbf{I}}_{\varphi,\pi} &= \hat{\mathbf{C}}_{vsc}\hat{\mathbf{X}}_{vsc} + \hat{\mathbf{F}}_{vsc}\hat{\mathbf{V}}_{\gamma,\pi} \end{cases} \quad (11)$$

The static transfer matrix $\hat{\mathbf{Y}}$ of the model (11) can be computed as $\hat{\mathbf{Y}} = \hat{\mathbf{C}}_{vsc}\left(j\Omega I - \hat{\mathbf{A}}_{vsc}\right)^{-1}\hat{\mathbf{E}}_{vsc} + \hat{\mathbf{F}}_{vsc}$ and has the dimension of an admittance matrix. $\hat{\mathbf{Y}}$ expresses the static relationship between the Fourier coefficients of $\hat{\mathbf{I}}_{\varphi,\pi}$ and $\hat{\mathbf{V}}_{\gamma,\pi}$ and has a fundamental role in the modeling of the frequency coupling effects due to the converter control nonlinearities.

By considering the harmonics until the $7^{th}$ order ($H_{max} = 7$), the block of $\hat{\mathbf{Y}}$ related to the positive Fourier images can be written as:

$$\begin{pmatrix} \hat{\mathbf{I}}_1 \\ \hat{\mathbf{I}}_2 \\ \hat{\mathbf{I}}_3 \\ \hat{\mathbf{I}}_4 \\ \hat{\mathbf{I}}_5 \\ \hat{\mathbf{I}}_6 \\ \hat{\mathbf{I}}_7 \end{pmatrix} = \begin{pmatrix} \hat{\mathbf{Y}}_{11} & \hat{\mathbf{Y}}_{12} & \hat{\mathbf{Y}}_{13} & \hat{\mathbf{Y}}_{14} & \hat{\mathbf{Y}}_{15} & \hat{\mathbf{Y}}_{16} & \hat{\mathbf{Y}}_{17} \\ \hat{\mathbf{Y}}_{21} & \hat{\mathbf{Y}}_{22} & \hat{\mathbf{Y}}_{23} & \hat{\mathbf{Y}}_{24} & \hat{\mathbf{Y}}_{25} & \hat{\mathbf{Y}}_{26} & \hat{\mathbf{Y}}_{27} \\ \hat{\mathbf{Y}}_{31} & \hat{\mathbf{Y}}_{32} & \hat{\mathbf{Y}}_{33} & \hat{\mathbf{Y}}_{34} & \hat{\mathbf{Y}}_{35} & \hat{\mathbf{Y}}_{36} & \hat{\mathbf{Y}}_{37} \\ \hat{\mathbf{Y}}_{41} & \hat{\mathbf{Y}}_{42} & \hat{\mathbf{Y}}_{43} & \hat{\mathbf{Y}}_{44} & \hat{\mathbf{Y}}_{45} & \hat{\mathbf{Y}}_{46} & \hat{\mathbf{Y}}_{47} \\ \hat{\mathbf{Y}}_{51} & \hat{\mathbf{Y}}_{52} & \hat{\mathbf{Y}}_{53} & \hat{\mathbf{Y}}_{54} & \hat{\mathbf{Y}}_{55} & \hat{\mathbf{Y}}_{56} & \hat{\mathbf{Y}}_{57} \\ \hat{\mathbf{Y}}_{61} & \hat{\mathbf{Y}}_{62} & \hat{\mathbf{Y}}_{63} & \hat{\mathbf{Y}}_{64} & \hat{\mathbf{Y}}_{65} & \hat{\mathbf{Y}}_{66} & \hat{\mathbf{Y}}_{67} \\ \hat{\mathbf{Y}}_{71} & \hat{\mathbf{Y}}_{72} & \hat{\mathbf{Y}}_{73} & \hat{\mathbf{Y}}_{74} & \hat{\mathbf{Y}}_{75} & \hat{\mathbf{Y}}_{76} & \hat{\mathbf{Y}}_{77} \end{pmatrix} \begin{pmatrix} \hat{\mathbf{V}}_1 \\ \hat{\mathbf{V}}_2 \\ \hat{\mathbf{V}}_3 \\ \hat{\mathbf{V}}_4 \\ \hat{\mathbf{V}}_5 \\ \hat{\mathbf{V}}_6 \\ \hat{\mathbf{V}}_7 \end{pmatrix}$$

Fundamental Components

Linear Time Invariant part of the model

Coupling terms between the fundamental voltage $\hat{\mathbf{V}}_1$ and the harmonic currents

Coupling terms between the harmonic voltages and the fundamental current $\hat{\mathbf{I}}_1$

(12)

The terms on the diagonal of (12), highlighted in green, describe the *linear* part of the VSC frequency response, already captured by conventional LTI impedance-based or state-space models [14], [32]. The off-diagonal terms represent

the coupling between different harmonic orders due to the system *nonlinearity*, not captured by LTI models. The study of the coupling between the harmonics and the fundamental frequencies is one of the primary goal of the paper. The terms highlighted in yellow in (12) put in relation the bus fundamental voltage and the current harmonics in the grid. Conversely, the red terms in (12) relate the bus harmonic voltage distortion and the converter fundamental current, i.e. its operating point.

### C. Harmonic Power Flow Framework

The considered HPF framework describes the power system by two sets of nodal equations, formulated from the point of view of the resources and the grid, respectively [8], [9]. All the equation are expressed in the $abc$ reference frame.

The grid nodes are divided into $\mathcal{R}$ nodes for grid following converters (as in Fig. 2) and passive loads, and $\mathcal{S}$ nodes for slack buses and grid forming converters. The equations from the point of view of the resources can be written as:

$$\hat{\mathbf{I}}_{\varphi,r} = \hat{\mathbf{Y}}_r \left( \hat{\mathbf{V}}_{\gamma,r}, w_{k,r} \right) \quad \text{for } r \in \mathcal{R} \tag{13}$$

$$\hat{\mathbf{V}}_{\gamma,s} = \hat{\mathbf{Z}}_s \left( \hat{\mathbf{I}}_{\varphi,s}, V_s^*, f_s^* \right) \quad \text{for } s \in \mathcal{S} \tag{14}$$

The linearization of (13) around the set-point defined by $w_{k,r}$ contains the frequency coupling terms of the converter internal response defined in (12). From the point of view of the grid, the nodal equations are formulated by the hybrid parameters:

$$\hat{\mathbf{I}}_{\varphi,\mathcal{R}} = \hat{\mathbf{H}}_{\mathcal{R}\times\mathcal{R}} \hat{\mathbf{V}}_{\gamma,\mathcal{R}} + \hat{\mathbf{H}}_{\mathcal{R}\times\mathcal{S}} \hat{\mathbf{I}}_{\varphi,\mathcal{S}} \tag{15}$$

$$\hat{\mathbf{V}}_{\gamma,\mathcal{S}} = \hat{\mathbf{H}}_{\mathcal{S}\times\mathcal{R}} \hat{\mathbf{V}}_{\gamma,\mathcal{R}} + \hat{\mathbf{H}}_{\mathcal{S}\times\mathcal{S}} \hat{\mathbf{I}}_{\varphi,\mathcal{S}} \tag{16}$$

where $\hat{\mathbf{H}}_{\mathcal{R}\times\mathcal{R}}$, $\hat{\mathbf{H}}_{\mathcal{R}\times\mathcal{S}}$, $\hat{\mathbf{H}}_{\mathcal{S}\times\mathcal{R}}$, $\hat{\mathbf{H}}_{\mathcal{S}\times\mathcal{S}}$ are the blocks of the hybrid transadmittance matrix associated with $\mathcal{R}$ and $\mathcal{S}$.

The frequency dependency of the network cable parameters in the nodal equations has been deeply discussed in [9], and it has been found that its impact on the magnitude of the lines admittance and on the results of the HPF analyses is negligible. Therefore, this paper considers cable models with frequency invariant parameters in (15)-(16).

At the equilibrium point, the mismatch between (13)-(14) and (15)-(16) must be null, i.e.:

$$\begin{cases} \Delta\hat{\mathbf{V}}_{\gamma,\mathcal{S}} = 0 \\ \Delta\hat{\mathbf{I}}_{\varphi,\mathcal{R}} = 0 \end{cases} \tag{17}$$

The mismatch equations (17) are solved by the HPF software through Newton-Raphson algorithm [8], [9].

## III. PLL-Synchronized Converter Linear Time Periodic Modeling

The modular modeling strategy used by the HPF framework allows to derive the models of each of the blocks in Fig. 2 separately, and to obtain a VSC internal response model in the form (11) by blocks interconnection. Each block can be expressed through a differential algebraic model such as (2), or through a simple algebraic input-output function (memoryless system).

The modeling of the control software $\kappa$ including the PLL and the reference frame transformation matrices is the main object of this section and one of the novelties of this paper with respect to [8], [9].

For the current reference calculation block $\rho$, two different strategies are considered. The first one is the constant power control (PQ-control), where the converters receive the active and reactive power set-points from the system-level controller and compute the current reference from it.

*PQ-controlled converters*:

$$w_\kappa = \begin{pmatrix} P^*(t) \\ Q^*(t) \end{pmatrix} \tag{18}$$

$$\begin{pmatrix} i^*_{\varphi_d}(t) \\ i^*_{\varphi_q}(t) \end{pmatrix} = \begin{pmatrix} \widetilde{v}_{\gamma_d}(t) & \widetilde{v}_{\gamma_q}(t) \\ \widetilde{v}_{\gamma_q}(t) & -\widetilde{v}_{\gamma_d}(t) \end{pmatrix}^{-1} w_\kappa \tag{19}$$

The second one is the constant current control, where the VSCs receive a current set-point from the system-level controller, thus their current reference calculation $\rho$ block is a unitary gain.

*Current-controlled converters*:

$$w_\kappa = \begin{pmatrix} i^*_{\varphi_d}(t) \\ i^*_{\varphi_q}(t) \end{pmatrix} \tag{20}$$

In the case of PQ-controlled converters, equation (19) represents a nonlinearity and generates frequency coupling terms. Since the modeling of this nonlinearity has been already discussed in [9], it is beyond the scope of this paper.

### A. Reference Frame Transformation model

The direct and inverse transformations between $abc$ and $dq$ reference frames (represented in Fig. 1 by single blocks) are treated in the proposed modeling strategy as two distinct cascaded blocks (as shown in a red frames in Fig. 2). The blocks $\tau_{\pi|\kappa}$ is aimed to synchronize the local $dq$ reference frame with the *fundamental* frequency $f_1$ of the three-phase $abc$ voltage $v_{\gamma_\pi}(t)$. The reference angle $\theta(t)$, used in $\tau_{\pi|\kappa}(\theta(t))$, can be therefore expressed as:

$$\theta(t) = 2\pi f_1 t + \theta_0 \tag{21}$$

where $\theta_0$ is known constant offset. Under this assumption, the reference frame transformation $\tau_{\pi|\kappa}(\theta)$ is:

$$\tau_{\pi|\kappa}(\theta(t)) = \sqrt{\frac{2}{3}} \begin{pmatrix} \cos(\theta(t)) & -\sin(\theta(t)) \\ \cos(\theta(t) - \frac{2\pi}{3}) & -\sin(\theta(t) - \frac{2\pi}{3}) \\ \cos(\theta(t) + \frac{2\pi}{3}) & -\sin(\theta(t) + \frac{2\pi}{3}) \end{pmatrix} \tag{22}$$

The block $\tau_{\kappa|\pi}(\theta(t)) = \tau_{\pi|\kappa}(\theta(t))^T$ realizes the inverse transformation. The matrix (22) introduces frequency coupling terms and its Fourier coefficients $\mathrm{T}_{\pi|\kappa_h}$ are computed as:

$$\begin{cases} \mathrm{T}_{\pi|\kappa_1} = \sqrt{\frac{2}{3}} \exp(j\theta_0) \begin{pmatrix} \frac{1}{2} & -\frac{1}{2j} \\ \frac{1}{2}\alpha^* & -\frac{1}{2j}\alpha^* \\ \frac{1}{2}\alpha & -\frac{1}{2j}\alpha \end{pmatrix} \\ \mathrm{T}_{\pi|\kappa_{(-1)}} = \mathrm{T}^*_{\pi|\kappa_1} \\ 0 \qquad \text{for} \quad h \neq 1 \text{ and } h \neq -1 \end{cases} \tag{23}$$

where $\alpha = \exp\left(j\frac{2\pi}{3}\right)$.

The effect of the harmonics of the grid voltage $v_\gamma$ on the synchronization angle $\theta$ is not considered in (21) [8], [9], nevertheless its existence and relevance is well-documented in the literature [25] and the modeling of its effect is one of the main target of this paper.

A zero-average periodic signal $\Delta\theta(t)$ is added to (21), resulting in the new synchronization angle $\widetilde{\theta}$, which takes the aforementioned effect into account:

$$\widetilde{\theta}(t) = 2\pi f_1 t + \theta_0 + \Delta\theta(t) = \theta(t) + \Delta\theta(t) \tag{24}$$

The variables expressed in the reference frame synchronized with $\widetilde{\theta}(t)$ are marked in this paper with $\widetilde{\square}$ (e.g. $\widetilde{v}_\gamma$), while variables in the reference frame synchronized with $\theta(t)$ are not marked (e.g. $v_\gamma$), as clear from Fig. 2.

The addition of $\Delta\theta(t)$ to $\theta(t)$ in (24) is modeled through the $dq$ rotation matrices $T(\Delta\theta(t))$ and $T^{-1}(\Delta\theta(t))$

$$T(\Delta\theta(t)) = \begin{pmatrix} \cos(\Delta\theta(t)) & \sin(\Delta\theta(t)) \\ -\sin(\Delta\theta(t)) & \cos(\Delta\theta(t)) \end{pmatrix} \tag{25}$$

cascaded with $\tau_{\kappa|\pi}(\theta(t))$ and $\tau_{\pi|\kappa}(\theta(t))$, as in Fig. 2.

The frequency coupling terms introduced by the PLL synchronization are due to $T(\Delta\theta(t))$ and $T^{-1}(\Delta\theta(t))$. By applying the rotation matrix (25) to the grid voltage $v_\gamma$, and considering the approximations $\cos(\Delta\theta(t)) \approx 1$, $\sin(\Delta\theta(t)) \approx \theta(t)$ assuming $\Delta\theta(t)$ small enough, the following expression is obtained:

$$\begin{pmatrix} \widetilde{v}_{\gamma_d}(t) \\ \widetilde{v}_{\gamma_q}(t) \end{pmatrix} = \begin{pmatrix} 1 & \Delta\theta(t) \\ -\Delta\theta(t) & 1 \end{pmatrix} \begin{pmatrix} v_{\gamma_d}(t) \\ v_{\gamma_q}(t) \end{pmatrix} \tag{26}$$

In (26), the nonlinearity given by the product of $\Delta\theta(t)$ and $v_\gamma(t)$ appears. According to section II, (26) can be linearized around the time-periodic equilibrium trajectory of the variables $\Delta\theta(t)$ and $v_\gamma(t)$, indicated with $\Delta\bar{\Theta}(t)$ and $\bar{V}_\gamma(t)$ respectively. By defining:

$$D_\Theta(t) = \begin{pmatrix} 1 & \Delta\bar{\Theta}(t) \\ -\Delta\bar{\Theta}(t) & 1 \end{pmatrix} \tag{27}$$

the function (26) can be linearized as:

$$\begin{cases} \begin{pmatrix} \widetilde{v}_{\gamma_d}(t) \\ \widetilde{v}_{\gamma_q}(t) \end{pmatrix} & = D_\Theta(t) \begin{pmatrix} v_{\gamma_d}(t) \\ v_{\gamma_q}(t) \end{pmatrix} + D_{dir_\gamma}(t)\Delta\theta(t) \\ D_{dir_\gamma}(t) & = \begin{pmatrix} \bar{V}_{\gamma_q}(t) \\ -\bar{V}_{\gamma_d}(t) \end{pmatrix} \end{cases} \tag{28}$$

An analogous expression can be written for the direct transformation of the converter filter current $i_\varphi$:

$$\begin{cases} \begin{pmatrix} \widetilde{i}_{\varphi_d}(t) \\ \widetilde{i}_{\varphi_q}(t) \end{pmatrix} & = D_\Theta(t) \begin{pmatrix} i_{\varphi_d}(t) \\ i_{\varphi_q}(t) \end{pmatrix} + D_{dir_\varphi}(t)\Delta\theta(t) \\ D_{dir_\varphi}(t) & = \begin{pmatrix} \bar{I}_{\varphi_q}(t) \\ -\bar{I}_{\varphi_d}(t) \end{pmatrix} \end{cases} \tag{29}$$

The linearized inverse transformation of the actuator voltage $v_\alpha$ is obtained by the same mathemathical procedure, considering the inverse (transpose) $T(\Delta\theta(t))^{-1}$ matrix in (26), obtaining:

$$\begin{cases} \begin{pmatrix} v_{\alpha_d}(t) \\ v_{\alpha_q}(t) \end{pmatrix} & = D_\Theta^T(t) \begin{pmatrix} \widetilde{v}_{\alpha_d}(t) \\ \widetilde{v}_{\alpha_q}(t) \end{pmatrix} - D_{inv_\alpha}(t)\Delta\theta(t) \\ D_{inv_\alpha}(t) & = \begin{pmatrix} \bar{V}_{\alpha_q}(t) \\ -\bar{V}_{\alpha_d}(t) \end{pmatrix} \end{cases} \tag{30}$$

The Fourier series expansion of the periodic matrices defined in (27)-(30) can be computed as:

$$\begin{cases} D_\Theta(t) & = \sum_{h=-N}^{N} D_{\Theta,\mathbf{h}} \exp(jh2\pi f_1 t) \\ D_{dir_\gamma}(t) & = \sum_{h=-N}^{N} D_{dir_{\gamma,\mathbf{h}}} \exp(jh2\pi f_1 t) \\ D_{dir_\xi}(t) & = \sum_{h=-N}^{N} D_{dir_{\xi,\mathbf{h}}} \exp(jh2\pi f_1 t) \\ D_{inv_\alpha}(t) & = \sum_{h=-N}^{N} D_{inv_{\alpha,\mathbf{h}}} \exp(jh2\pi f_1 t) \end{cases} \tag{31}$$

### *B. Modeling of synchronization $\sigma$ and current control $\xi$*

The synchronization block $\sigma$ in Fig. 2 models the effect of the input voltage $v_\gamma$ harmonics on the angle $\Delta\theta$. This paper considers a traditional Synchronous Reference Frame PLL (SRF-PLL), whose model is LTI and well-known in literature [7], [32]:

$$\begin{cases} \begin{pmatrix} \dot{\Delta\theta} \\ \dot{\Phi}_\gamma \end{pmatrix} & = \begin{pmatrix} 0 & K_{i,PLL} \\ 0 & 0 \end{pmatrix} \begin{pmatrix} \Delta\theta \\ \Phi_\gamma \end{pmatrix} + \begin{pmatrix} 0 & K_{p,PLL} \\ 0 & 1 \end{pmatrix} \begin{pmatrix} \widetilde{v}_{\gamma_d}(t) \\ \widetilde{v}_{\gamma_q}(t) \end{pmatrix} \\ \Delta\theta & = \begin{pmatrix} 1 & 0 \end{pmatrix} \begin{pmatrix} \Delta\theta \\ \Phi_\gamma \end{pmatrix} \end{cases} \tag{32}$$

where $K_{p,PLL}$ and $K_{i,PLL}$ are the proportional and integral gain of the PLL PI regulator. The model (32) is indicated in this paper with the compact notation:

$$\begin{cases} \dot{x}_\sigma & = A_\sigma x_\sigma + B_\sigma \widetilde{v}_{\gamma,\kappa}(t) \\ \Delta\theta & = C_\sigma x_\sigma \end{cases} \tag{33}$$

The model of the current controller $\xi$ is also LTI and is also well-known in literature [9]:

$$\begin{cases} \dot{x}_\xi & = A_\xi x_\xi + B_\xi \widetilde{i}_\varphi(t) + E_\xi i_\varphi^*(t) \\ \widetilde{v}_\alpha & = C_\xi x_\xi + D_\xi \widetilde{i}_\varphi(t) + F_\xi i_\varphi^*(t) \end{cases} \tag{34}$$

with

$$\begin{cases} A_\xi = 0_{2\times2} \quad B_\xi = -I_{2\times2} \quad E_\xi = I_{2\times2} \\ C_\xi = K_i I_{2\times2} \quad D_\xi = -K_p I_{2\times2} \quad F_\xi = K_p I_{2\times2} \end{cases} \tag{35}$$

where $K_p$ and $K_i$ are the proportional and integral gain of the current PI regulator. The considered converter switching frequency is 10 kHz, and the harmonics until the $7^{th}$ order are considered in the study, which justifies the assumption of neglecting the switching effect, as in [8], [9], [33].

### *C. Full control software model by blocks interconnection*

The state-space interconnected model of the whole control software model $\kappa$ highlighted in green in Fig. 2 can be

obtained by interconnecting the different blocks. As discussed in section II, its linearization results in a LTP system:

$$\begin{cases} \begin{pmatrix} \dot{x}_\xi(t) \\ \dot{x}_\sigma(t) \end{pmatrix} = A_\kappa(t) \begin{pmatrix} x_\xi(t) \\ x_\sigma(t) \end{pmatrix} + B_\kappa(t) \begin{pmatrix} i_{\varphi,\kappa}(t) \\ v_{\gamma,\kappa}(t) \end{pmatrix} + E_\kappa(t) i^*_\varphi(t) \\ v_\alpha = C_\kappa(t) \begin{pmatrix} x_\xi(t) \\ x_\sigma(t) \end{pmatrix} + D_\kappa(t) \begin{pmatrix} i_{\varphi,\kappa}(t) \\ v_{\gamma,\kappa}(t) \end{pmatrix} + F_\kappa(t) i^*_\varphi(t) \end{cases} \tag{36}$$

with

$$\begin{cases} A_\kappa(t) = \begin{pmatrix} A_\xi & B_\xi D_{dir_\varphi}(t) C_\sigma \\ 0 & A_\sigma + B_\sigma D_{dir_\gamma}(t) C_\sigma \end{pmatrix} \\ B_\kappa(t) = \begin{pmatrix} B_\xi(I + D_\Theta(t)) & 0 \\ 0 & B_\sigma(I + D_\Theta(t)) \end{pmatrix} \\ C_\kappa(t) = \begin{pmatrix} C_\xi & D_\xi D_{dir_\varphi}(t) C_\sigma + D_{inv_\alpha}(t) C_\sigma \end{pmatrix} \\ D_\kappa(t) = D_\xi(I + D_\Theta(t)) \\ E_\kappa = \begin{pmatrix} E_\xi \\ 0 \end{pmatrix} \\ F_\kappa = F_\xi \end{cases} \tag{37}$$

The model time-periodicity is due to the periodic terms $D_{dir_\gamma}(t)$, $D_{dir_\varphi}(t)$, $D_{inv_\alpha}(t)$ defined in (28)-(30) appearing inside the linearized matrices $A_\kappa(t)$, $B_\kappa(t)$, $C_\kappa(t)$ and $D_\kappa(t)$ in (37). The Fourier coefficients of the matrices (37) are:

For $h = 0$:

$$\begin{cases} A_{\kappa_\mathbf{0}} = \begin{pmatrix} A_\xi & B_\xi D_{dir_{\varphi,\mathbf{0}}} C_\sigma \\ 0 & A_\sigma + B_\sigma D_{dir_{\gamma,\mathbf{0}}} C_\sigma \end{pmatrix} \\ B_{\kappa_\mathbf{0}} = \begin{pmatrix} B_\xi D_{\Theta,\mathbf{0}} & 0 \\ 0 & B_\sigma D_{\Theta,\mathbf{0}} \end{pmatrix} \\ C_{\kappa_\mathbf{0}} = \begin{pmatrix} C_\xi & D_\xi D_{dir_{\varphi,\mathbf{0}}} C_\sigma + D_{inv_{\alpha,\mathbf{0}}} C_\sigma \end{pmatrix} \\ D_{\kappa_\mathbf{0}} = D_\xi D_{\Theta,\mathbf{0}} \\ E_{\kappa_\mathbf{0}} = \begin{pmatrix} E_\xi \\ 0 \end{pmatrix} \\ F_{\kappa_\mathbf{0}} = F_\xi \end{cases} \tag{38}$$

For $h \neq 0$:

$$\begin{cases} A_{\kappa_\mathbf{h}} = \begin{pmatrix} 0 & B_\xi D_{dir_{\varphi,\mathbf{h}}} C_\sigma \\ 0 & B_\sigma D_{dir_{\gamma,\mathbf{h}}} C_\sigma \end{pmatrix} \\ B_{\kappa_\mathbf{h}} = \begin{pmatrix} B_\xi D_{\Theta,\mathbf{h}} & 0 \\ 0 & B_\sigma D_{\Theta,\mathbf{h}} \end{pmatrix} \\ C_{\kappa_\mathbf{h}} = \begin{pmatrix} 0 & D_\xi D_{dir_{\varphi,\mathbf{h}}} C_\sigma + D_{inv_{\alpha,\mathbf{h}}} C_\sigma \end{pmatrix} \\ D_{\kappa_\mathbf{h}} = D_\xi D_{\Theta,\mathbf{h}} \\ E_{\kappa_\mathbf{h}} = \begin{pmatrix} 0 \\ 0 \end{pmatrix} \\ F_{\kappa_\mathbf{h}} = 0 \end{cases} \tag{39}$$

From the Fourier coefficients (38)-(39), the harmonic state-space model in the form (8) can be built and embedded in the HPF software [8], [9]. In order to get the equilibrium trajectory of the state $\bar{x}_\kappa(t) = \begin{pmatrix} \bar{x}_\xi(t) & \bar{x}_\sigma(t) \end{pmatrix}^T$, the derivative $\dot{x}_\kappa(t)$ in (36) has to be set to 0, and the resulting algebraic linear system has to be solved in $x_\kappa$ [7].

It is important to observe that the frequency coupling terms generated by the reference frame transformation depend on: (i) the PLL tuning through the terms $B_\sigma$ and (ii) the current controller gains through the term $D_\xi$ in the Fourier coefficients (39). The prominent cross-coupling between the current controller and the PLL dynamics in the synchronization process in weak grid has been highlighted in several recent studies [32], [34], [35].

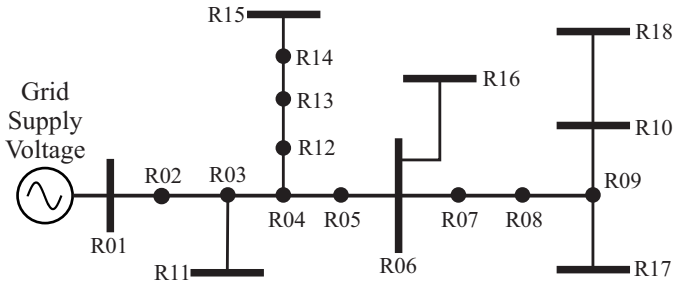


Fig. 3: The Cigré 18-bus benchmark distribution grid considered for the Harmonic Power Flow analysis [29], [36].

TABLE I: Line Configuration

| Line name | From | To | Cable type | Length (m) |
|---|---|---|---|---|
| L-01 | R01 | R02 | UG-01 | 105 |
| L-02 | R02 | R03 | UG-01 | 105 |
| L-03 | R03 | R04 | UG-01 | 105 |
| L-04 | R04 | R05 | UG-01 | 105 |
| L-05 | R05 | R06 | UG-01 | 105 |
| L-06 | R06 | R07 | UG-01 | 105 |
| L-07 | R07 | R08 | UG-01 | 105 |
| L-08 | R08 | R09 | UG-01 | 105 |
| L-09 | R09 | R10 | UG-01 | 105 |
| L-10 | R03 | R11 | UG-04 | 90 |
| L-11 | R04 | R12 | UG-02 | 105 |
| L-12 | R12 | R13 | UG-02 | 105 |
| L-13 | R13 | R14 | UG-02 | 105 |
| L-14 | R14 | R15 | UG-02 | 90 |
| L-15 | R06 | R16 | UG-06 | 90 |
| L-16 | R09 | R17 | UG-04 | 90 |
| L-17 | R10 | R18 | UG-05 | 90 |

## IV. Harmonic Power Flow Analysis

The considered 18-bus distribution grid is depicted in Fig. 3. The grid topology and the cable types are adopted from the Cigré benchmark grid in [29]; compared with the original benchmark grid, the lengths of the cables are increased by three times to obtain a weak grid (see Table I). The maximum distance from the slack bus (from R01 to R18) is around 1 km, which is realistic for a low voltage network. The electrical parameters of the different cable types are shown in Table II. The lines $R/X$ ratio is high, which is a typical characteristic for low voltage distribution grids.

Different kinds of loads and generators are connected to the grid buses, as reported in Table III (passive sign convention has been adopted). The values are expressed in per unit with respect to the base power $P_b = 1$ kW and base voltage $V_b = 325$V. Two VSCs interfacing battery energy storage systems (BESS) are connected to the buses R06 and R10, operating with a power factor (PF) 0.8. A VSC-interfaced

TABLE II: Cable Types

| **Cable type** | $R'(\Omega/\text{km})$ | $X'(\Omega/\text{km})$ | $R'/X'$ ratio |
|---|---|---|---|
| UG-01 | 0.163 | 0.136 | 1.199 |
| UG-02 | 0.266 | 0.151 | 1.762 |
| UG-04 | 1.541 | 0.206 | 7.481 |
| UG-05 | 1.111 | 0.195 | 5.691 |
| UG-06 | 0.569 | 0.174 | 3.270 |

TABLE III: Generation and load configuration for $k_l = 1$ (per phase, balanced)

| **Bus/Load** | $\Re(Y_k)$ | $\Im(Y_k)$ | $\lvert I_k\rvert$ | $\angle I_k$ | $P_k$ | $Q_k$ |
|---|---|---|---|---|---|---|
| R-06 | - | - | - | - | -81.54 | -61.15 |
| R-10 | - | - | 102.09 | 31.95 | -81.54 | -61.15 |
| R-11 | - | - | 50.96 | 36.87 | 86.63 | 54.02 |
| R-15 | - | - | - | - | -101.92 | 0 |
| R-16 | 50.96 | -50.96 | - | - | 86.63 | 54.02 |
| R-17 | 0 | 20.38 | - | - | 86.63 | 54.02 |
| R-18 | - | - | - | - | 0 | -31.60 |

Distributed Energy Resource (DER) operating at unity power factor is connected at bus R15, while a Static synchronous Compensator (STATCOM) is connected to bus R18 to support the grid voltage. PQ-controlled converters interfacing DC loads are connected to bus R11, R16 and R17, current-controlled converters are connected to R10 and R11 and passive loads are connected to the bus R16 and R17, according to Table III. The distribution grid is connected to a main supply grid at bus R1, assumed with a total harmonic distortion (THD) of the voltage equal to 7.81%.

In order to analyze the grid under different operating conditions, it is assumed that all the resources in Table III (loads and generators) are multiplied by a scaling factor $k_l$, denominated *grid loadability factor*.

### A. Proposed PLL-synchronized converter LTP model validation

Before realizing HPF analyses of the distribution grid in Fig. 3, the proposed converter LTP model has to be validated. The validation is carried out by comparing the results obtained by the HPF software with the steady-state harmonic spectra obtained by a time-domain simulation (TDS) in Simulink®. The harmonics until the $25^{th}$ order are considered in the result. The spectra of the TDS are computed through a Discrete Fourier Transform (DFT) applied to a time-window of 5 periods of the fundamental frequency. The results in the left side of Fig. 4 show a good accuracy of the HPF with respect to the TDS. To better quantify the accuracy, two Key Performance Indicators (KPIs) are defined as the errors between the harmonics phasors obtained by the HPF and the TDS [9]:

$$\begin{cases} e_{\text{abs}}(I_{\varphi,h}) = \max_p \| |I_{\varphi,h,p,HPF}| - |I_{\varphi,h,p,TDS}| \| \\ e_{\text{arg}}(I_{\varphi,h}) = \max_p \| \angle I_{\varphi,h,p,HPF} - \angle I_{\varphi,h,p,TDS} \| \end{cases} \quad (40)$$

Thus, $e_{\text{abs}}$ and $e_{\text{arg}}$ are the maximum absolute errors over all the phases $p \in \mathcal{P}$ in magnitude and phase, respectively. The graphs in the right side of Fig. 4 show the errors between the HPF and the Simulink®model in terms of the KPIs defined in (40). The maximum values of the KPIs are $e_{\text{abs}}(I_{\varphi,17}) = 1.21E\text{-}3$ p.u. and $e_{\text{arg}}(I_{\varphi,13}) = 0.32$ deg, highlighted with red lines in Fig. 4. These errors are below the accuracy of standard measurement equipment and are therefore negligible.

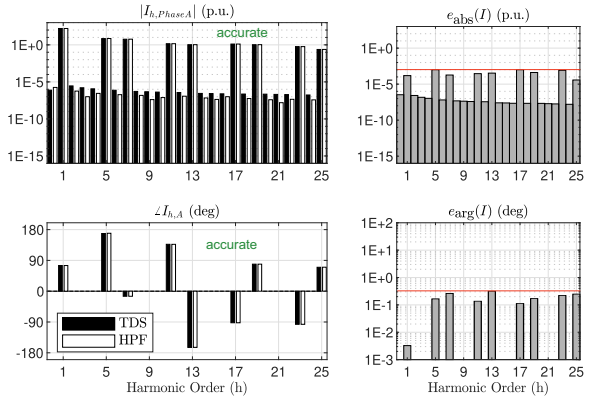


Fig. 4: Validation of the proposed LTP converter model by comparison with a time-domain simulation model.

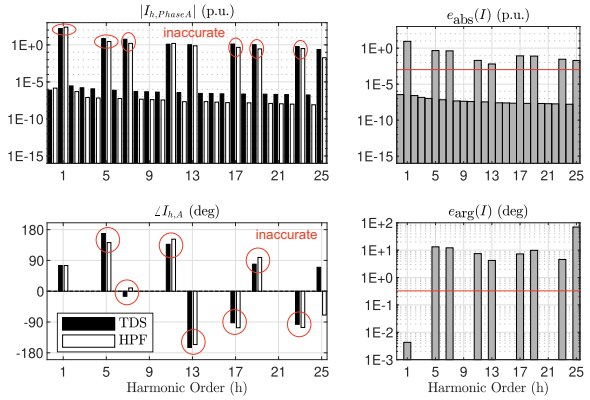


Fig. 5: Inaccuracy of the conventional LTI converter model by comparison with a time-domain simulation model.

The same tests have been carried out in Fig. 5 with a conventional LTI model, built by linearizing the converter state-space model around its nominal *undistorted* operating point ($V_\gamma = 1$ p.u.) [11], [14]. The inaccuracy of LTI model can be clearly seen in Fig. 5, both in the harmonics amplitudes and phases. This result further motivates the importance of LTP models for the realization of accurate HPF analyses. The current waveform obtained from the time-domain simulation in the tests of Figs. 4, 5 is shown in Fig. 6.

### B. Effect of frequency coupling on the power system

The frequency coupling between fundamental and harmonic quantities, explained in (12) at converter-level, has important implications at power system-level. Stability issues such as voltage instability, which are conventionally studied by only considering the fundamental quantities (bus voltages, active and reactive powers), are effectively dependent also on the harmonics, because of their coupling with the fundamental. In the following results, the harmonics until the $7^{th}$ order are considered in the grid supply voltage.

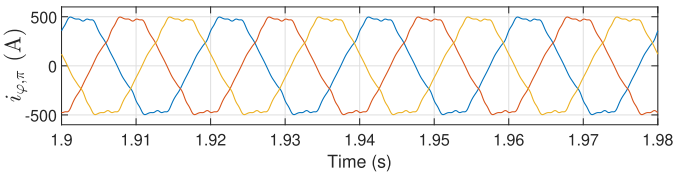


Fig. 6: The waveform of the converter current in the time-domain validation of the proposed converter LTP model.

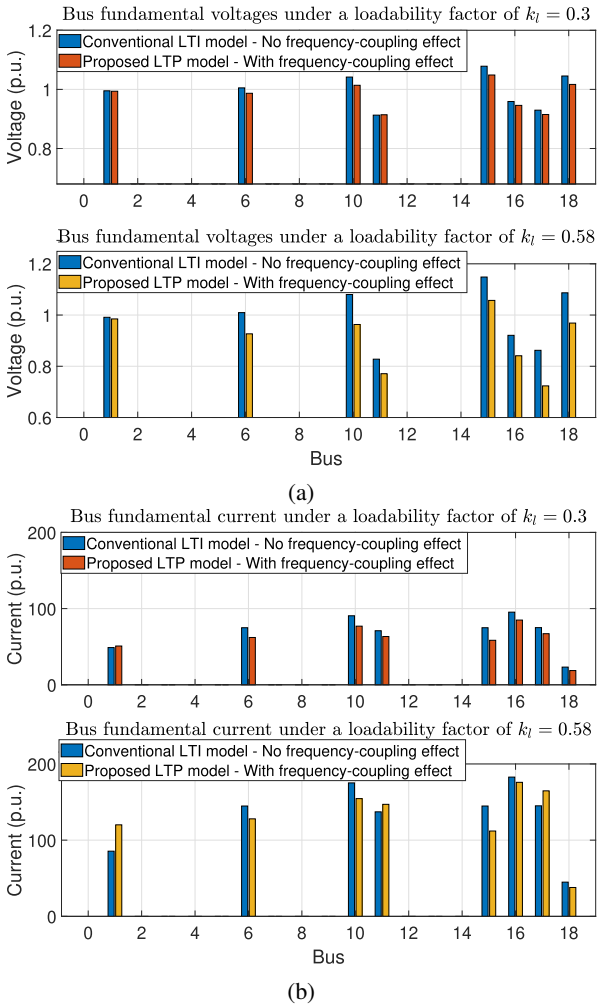


(a)

(b)

Fig. 7: The frequency coupling effects on the fundamental seen through HPF. (a) Bus fundamental voltages. (b) Bus fundamental currents.

In Fig. 7, bus fundamental voltages and current injections are shown for a medium loadability level $k_l = 0.3$ and a high loadability level $k_l = 0.58$, comparing conventional LTI models and proposed LTP models for power converters. The maximum loadability limit of the considered 18-bus grid is computed as $k_l = 0.62$ by the HPF and validated through a time-domain simulation model.

The fundamental voltage at the buses where loads are connected tend to decrease in high loadability conditions [15], [37]. In harmonic polluted scenarios, however, it is found that the fundamental voltages of the buses are lower in the HPF analyses using LTP models with respect to LTI models, as

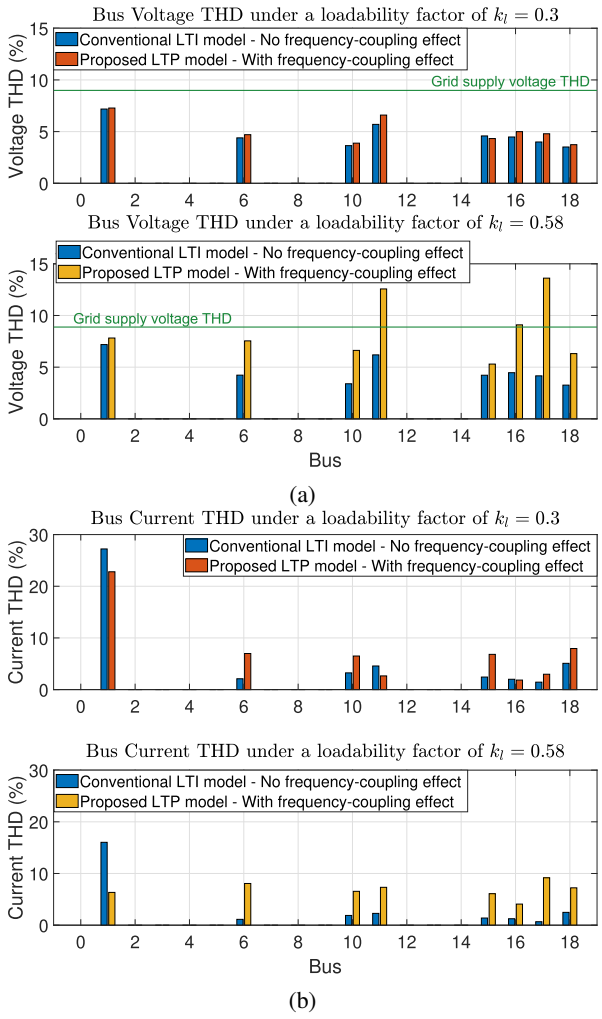


(a)

(b)

Fig. 8: The frequency coupling effects on the harmonics seen through HPF. (a) Bus voltages THD. (b) Bus currents THD.

shown in Fig. 7(a). The difference is much more prominent in high loadability conditions ($k_l = 0.58$). This is partly due to the fact that the used LTI converter models do not consider the nonlinear constant power behaviour of the VSCs, and partly due to the coupling between harmonic frequencies, object of this paper.

The frequency coupling terms highlighted in red in (12) couple the fundamental current (related to the loadability) to the voltage harmonics, resulting in higher voltage THD in high loadability condition, confirmed by Fig. 8(a) with LTP models. Higher harmonic voltages results in higher harmonic currents, confirmed by Fig. 8(b). Higher harmonic currents flowing in the network decrease the bus fundamental voltages because of the coupling terms highlighted in yellow in (12), representing therefore a *burden* for the system.

The reduction of the bus fundamental voltages due to harmonics is further confirmed by the test in Fig. 9. A high loadability condition ($k_l = 0.58$) is considered and the proposed LTP converter models are used in the HPF framework. The bus fundamental voltages and currents are compared in a scenario without harmonics in the grid supply voltage (represented by

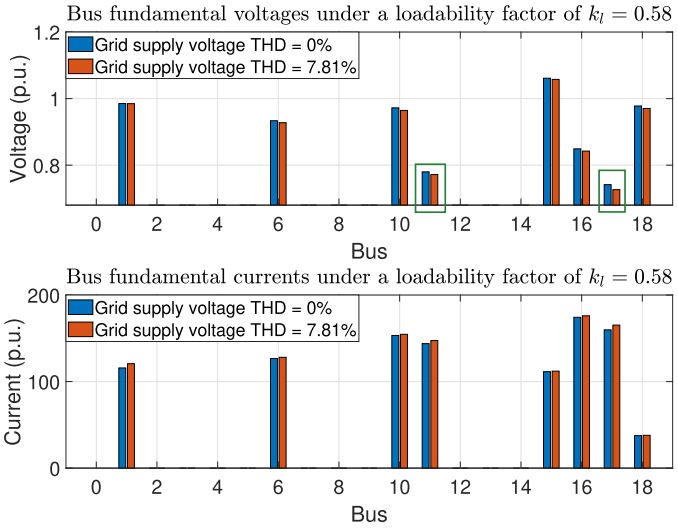


Fig. 9: The reduction of the buses fundamental voltage due to the frequency coupling terms in harmonic polluted networks.

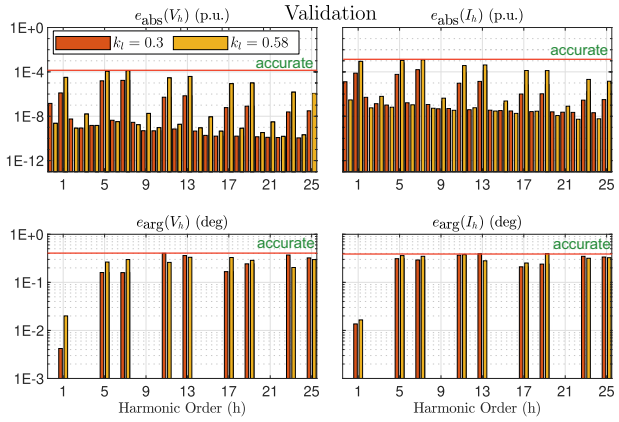


Fig. 10: Validation of the HPF analysis in Figs. 7 and 8 by comparison with the time-domain simulation of the benchmark grid.

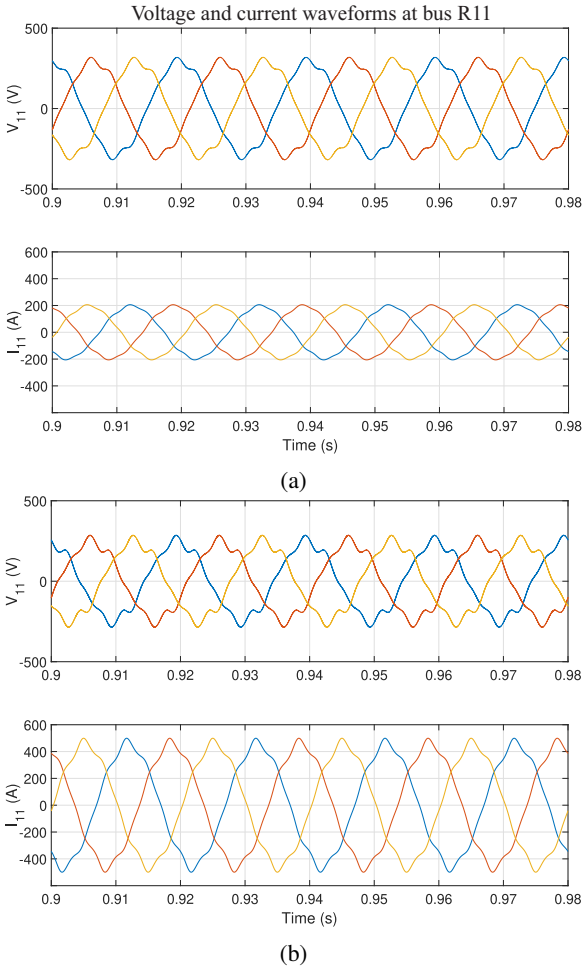


Fig. 11: The frequency coupling effects seen through time-domain simulation of the grid. (a) Bus R11 for $k_l = 0.3$. (b) Bus R11 for $k_l = 0.58$.

the blue bars) and a scenario with a THD = 7.81% (represented by the orange bars). The buses voltage reduction in harmonic polluted conditions can be clearly noticed in Fig. 9, and can reach 0.02 p.u. in heavily loaded buses with already low fundamental voltage. This phenomenon is relevant in voltage stability studies, since it majorly affects the buses which have already a high risk of voltage instability [15], [16].

As a matter of fact, the described frequency coupling phenomena are not captured by conventional LTI models, yet they create a "vicious cycle" which can significantly deteriorate the grid power quality and operation. These phenomena are more prone to occur at *high loadability conditions* ($k_l = 0.58$) and with *distorted grid voltage* (THD = 7.81%). Under these conditions, the power transmission is no longer predominantly at the fundamental frequency $f_1$, but it redistributes itself on a wider harmonic frequency spectrum, as clear from the increased current THD in Fig. 8(b).

Besides contributing to the bus voltage reduction, the power converter nonlinearity acts as a *harmonic amplifier* analogously to conventional nonlinear loads, as highlighted in Fig. 8(a), and can result in bus voltages THDs even higher than the grid supply voltage THD. This prominent nonlinear harmonic amplification is also not captured by conventional LTI models.

The HPF analyses carried out in Figs. 7 and 8 are further validated by comparing the results with a time-domain simulation of the considered distribution grid. The maximum absolute errors of voltages and currents over all buses, quantified through the KPI defined in (40), are depicted in Fig. 10. The validation is done both in the case of medium loadability condition ($k_l = 0.3$) and high loadability conditions ($k_l = 0.58$).

The results show that the maximum errors are $e_{\text{abs}}(I_{\varphi,7}) = 2.04E\text{-}3$ p.u. for the magnitude at bus R17 and $e_{\text{arg}}(V_{\gamma,7}) = 0.41$ deg for the phase at bus R17, highlighted with red lines in Fig. 4. The errors are generally higher in high loadability condition ($k_l = 0.58$), because when the grid approaches the voltage stability limit the HPF problem becomes more and more ill-conditioned [15], [16]. Nevertheless, even in high loadability condition, the maximum errors shown in Fig. 4 are below the accuracy of standard measurement equipment, and the validity of the analyses in Figs. 7 and 8 is thus confirmed.

The voltage harmonic amplification phenomenon in Fig.

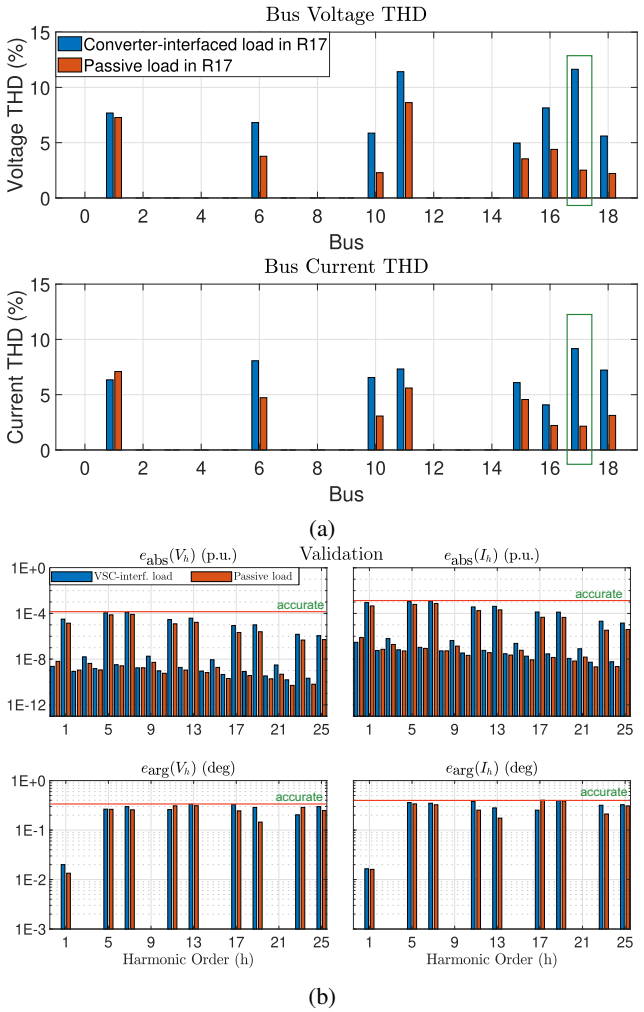


Fig. 12: The comparison of the grid harmonic distortion with a converted-interfaced load and a linear passive load. (a) Harmonic Power Flow results. (b) Validation of the results by comparison with time-domain simulation.

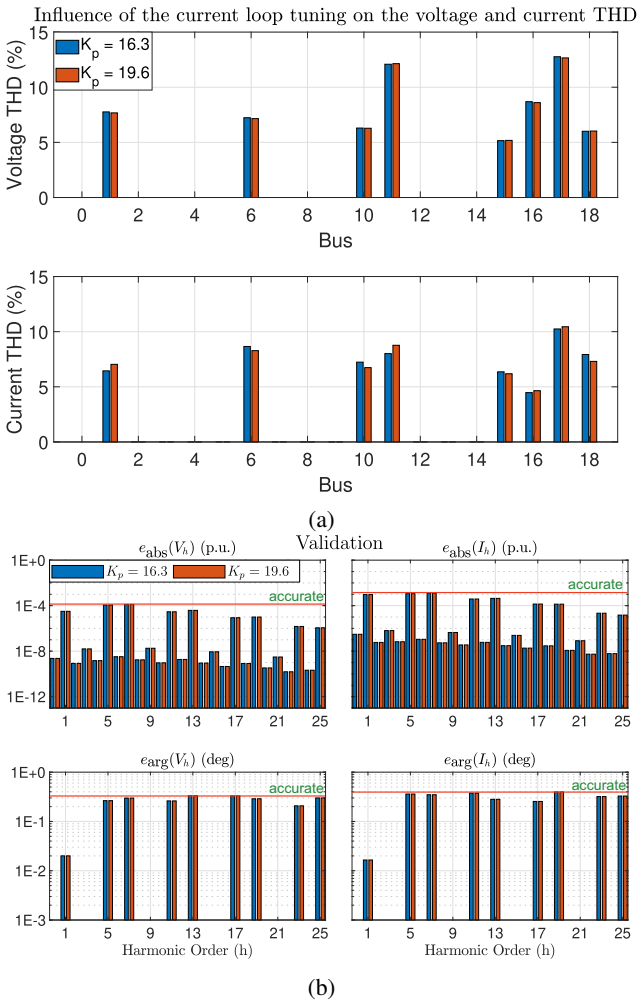


Fig. 13: The influence of the current loop tuning on the bus voltages and currents THD. (a) Harmonic Power Flow results. (b) Validation of the results by comparison with time-domain simulation.

8(a) is further confirmed by the waveforms obtained from the grid time-domain simulation. In Fig. 11 the voltage and current waveforms at the bus R11 are shown both under medium ($k_l = 0.3$) and high ($k_l = 0.58$) loadability condition. The harmonic content is significantly higher in Fig. 11(b) with respect to Fig. 11(a), which confirms that high loading levels results in increased harmonic distortion in power electronics-dominated grids connected to a distorted supply grid.

In Fig. 12(a), the effect on the harmonics of converter-interfaced loads and linear passive loads are compared in high loadability condition ($k_l = 0.58$). The load configuration in Table III is modified by substituting the PQ-controlled converter-interfaced load in bus R17 with a passive RL load absorbing an *identical* power. The new load configuration is compared with the original one in Table III through a HPF analysis, as shown in Fig. 12(a). It emerges that a converted-interfaced load connected to the grid results in significantly higher harmonic distortion than a passive load with the same power. The effect is more prominent in the bus R17 at which the load is connected, but it propagates also the in the rest of the grid. This results further highlights the harmonic detrimental effect of grid-connected VSCs. The validation of the result in Fig. 12(a) is presented in Fig. 12(b), which shows absolute errors in magnitude and phase in the same extent of Fig. 10, confirming the validity of the analysis.

### C. *Effect of the control tuning on the power system harmonics*

The effect of the tuning of the current controller $\xi$ and synchronization $\sigma$ on the power system harmonics is investigated through HPF analysis in Figs. 13, 14 for a grid loadability factor $k_l = 0.58$. The current control proportional gain $K_p$ and the PLL gains $K_{p,PLL}$, $K_{i,PLL}$ are contained in the matrices $D_\xi$, $B_\sigma$, $A_\sigma$ in (35), (32), respectively. Thus, they are all involved in the expression of the Fourier coefficients (39), which are responsible of the frequency coupling mechanism. The control parameters $K_p$, $K_{p,PLL}$, $K_{i,PLL}$ are, however, also involved on the small-signal stability of the grid, which cannot be assessed through a static HPF model [7]. To ensure the validity of the following HPF analyses, the grid stability must be verified through a dynamic small-signal analysis or a

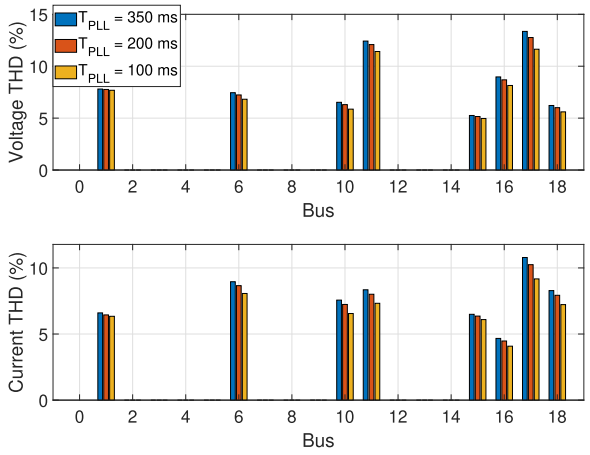


Fig. 14: The influence of the PLL tuning on the bus voltages and currents THD.

time-domain simulation, for all the considered control tunings [7].

The tuning of the $K_p$ is conventionally based on the desired phase margin and the delay introduced by the Pulse Width Modulation (PWM) and the digital computation [1]. However, grid impedance variations have also an influence on the current control dynamics, thus they need to be considered in the tuning process [35]. In Fig. 13(a), the effect of a 20% increase of the current loop proportional gain $K_p$ of all the converters is investigated. The variation of $K_p$ has a small effect on the bus voltage THD, but it has a relevant effect on the bus current THD. Increasing the $K_p$ brings a decreased current THD in R06, R10, R15 and R18, and an increased current THD in R01, R11 and R17. The behaviour of the bus current THD with respect to the $K_p$ depends on a number of factors, including grid configuration, converter control strategy (PQ-controlled or current-controlled converters), operating mode (generator or load), and cable parameters among them.

The influence of the PLL tuning on the grid harmonics is shown in Fig. 14. The PLL tuning is realized according to the procedure in [1], which aims to obtain a desired settling time $T_{PLL}$ with optimally damped dynamics. Different choices of $T_{PLL}$ result in different $K_{p,PLL}$ and $K_{i,PLL}$, which affect the harmonic propagation in the grid, as shown in Fig. 14. By decreasing $T_{PLL}$ (increasing $K_{p,PLL}$ and $K_{i,PLL}$) both the voltage and the current THD decrease in all the buses.

It is important to notice that, a 20% variation of the current loop gain in Fig. 13(a) has an effect on the current THD comparable to a 350% variation of the PLL settling time in Fig. 14. The current THD is thus more sensible to the current loop tuning than the PLL tuning. The validation of the result in Fig. 13(a) is presented in Fig. 13(b), confirming also in this case the validity of the analysis.

## V. Conclusions

This paper proposes a Linear Time Periodic model of a PLL-synchronized converter for Harmonic Power Flow studies. The proposed model captures the effects of the converter nonlinearities due to the control system on the grid steady-state operation. It is revealed that in high loadability conditions and with distorted grid supply voltage, the converter nonlinear response can have significant effects both on the fundamental and the harmonic bus voltages and currents, not captured by conventional LTI converters model. In particular, the harmonic voltages and currents are significantly amplified by the converter nonlinearities when the grid loadability factor increases. Moreover, the bus fundamental voltages may experience decrease till 0.02 p.u. due to the harmonic pollution, specially in heavily loaded buses, representing a risk for the voltage stability. The converters current loop and PLL tuning are also involved in the frequency coupling mechanism and have an influence on the harmonic distortion in the grid. The obtained results quantifies the importance of the frequency coupling terms introduced by the converter nonlinearity and the inaccuracy of conventional LTI converters models for harmonic power flow analyses.

## References

[1] R. Teodorescu, M. Liserre, and P. Rodriguez, *Grid converters for photovoltaic and wind power systems*, vol. 29. John Wiley & Sons, 2011.

[2] X. Wang and F. Blaabjerg, "Harmonic stability in power electronic-based power systems: Concept, modeling, and analysis," *IEEE Transactions on Smart Grid*, vol. 10, no. 3, pp. 2858–2870, May. 2019.

[3] J. Enslin and P. Heskes, "Harmonic interaction between a large number of distributed power inverters and the distribution network," *IEEE Transactions on Power Electronics*, vol. 19, no. 6, pp. 1586–1593, 2004.

[4] R. Redl, P. Tenti, and J. Daan van Wyk, "Power electronics' polluting effects," *IEEE Spectrum*, vol. 34, no. 5, pp. 32–39, 1997.

[5] M. Farrokhabadi, C. A. Cañizares, J. W. Simpson-Porco, E. Nasr, L. Fan, P. A. Mendoza-Araya, R. Tonkoski, U. Tamrakar, N. Hatziargyriou, D. Lagos, R. W. Wies, M. Paolone, M. Liserre, L. Meegahapola, M. Kabalan, A. H. Hajimiragha, D. Peralta, M. A. Elizondo, K. P. Schneider, F. K. Tuffner, and J. Reilly, "Microgrid stability definitions, analysis, and examples," *IEEE Transactions on Power Systems*, vol. 35, DOI 10.1109/TPWRS.2019.2925703, no. 1, pp. 13–29, 2020.

[6] F. Zare, H. Soltani, D. Kumar, P. Davari, H. A. M. Delpino, and F. Blaabjerg, "Harmonic emissions of three-phase diode rectifiers in distribution networks," *IEEE Access*, vol. 5, pp. 2819–2833, 2017.

[7] F. Cecati, R. Zhu, M. Liserre, and X. Wang, "Nonlinear modular state-space modeling of power-electronics-based power systems," *IEEE Transactions on Power Electronics*, vol. 37, no. 5, pp. 6102–6115, 2022.

[8] A. M. Kettner, L. Reyes-Chamorro, J. K. M. Becker, Z. Zou, M. Liserre, and M. Paolone, "Harmonic power-flow study of polyphase grids with converter-interfaced distributed energy resources—part i: Modeling framework and algorithm," *IEEE Transactions on Smart Grid*, vol. 13, no. 1, pp. 458–469, 2021.

[9] J. K. M. Becker, A. M. Kettner, L. Reyes-Chamorro, Z. Zou, M. Liserre, and M. Paolone, "Harmonic power-flow study of polyphase grids with converter-interfaced distributed energy resources—part ii: Model library and validation," *IEEE Transactions on Smart Grid*, vol. 13, no. 1, pp. 470–481, 2022.

[10] Y. Liao and X. Wang, "Small-signal modeling of ac power electronic systems: Critical review and unified modeling," *IEEE Open Journal of Power Electronics*, vol. 2, pp. 424–439, 2021.

[11] L. Harnefors, M. Bongiorno, and S. Lundberg, "Input-admittance calculation and shaping for controlled voltage-source converters," *IEEE Transactions on Industrial Electronics*, vol. 54, no. 6, pp. 3323–3334, 2007.

[12] F. Cecati, S. Pugliese, R. Zhu, and M. Liserre, "Integration and optimization of voltage active filtering functionality in a pv park," in *IECON 2019 - 45th Annual Conference of the IEEE Industrial Electronics Society*, vol. 1, pp. 4733–4739, 2019.

[13] F. Safargholi, K. Malekian, and W. Schufft, "On the dominant harmonic source identification— part i: Review of methods," *IEEE Transactions on Power Delivery*, vol. 33, DOI 10.1109/TPWRD.2017.2751663, no. 3, pp. 1268–1277, 2018.

[14] N. Pogaku, M. Prodanovic, and T. C. Green, "Modeling, analysis and testing of autonomous operation of an inverter-based microgrid," *IEEE TPEL*, vol. 22, no. 2, pp. 613–625, 2007.

[15] T. Van Cutsem and C. Vournas, *Voltage stability of electric power systems*. Springer Science & Business Media, 2007.
[16] A. M. Kettner and M. Paolone, "A generalized index for static voltage stability of unbalanced polyphase power systems including thévenin equivalents and polynomial models," *IEEE Transactions on Power Systems*, vol. 34, no. 6, pp. 4630–4639, 2019.
[17] M. O. Teixeira, I. D. Melo, and A. João Filho, "An optimisation model based approach for power systems voltage stability and harmonic analysis," *Electric Power Systems Research*, vol. 199, p. 107462, 2021.
[18] F. Yahyaie and P. W. Lehn, "Using frequency coupling matrix techniques for the analysis of harmonic interactions," *IEEE Transactions on Power Delivery*, vol. 31, no. 1, pp. 112–121, 2015.
[19] P. Lehn and K. Lian, "Frequency coupling matrix of a voltage-source converter derived from piecewise linear differential equations," *IEEE Transactions on Power Delivery*, vol. 22, no. 3, pp. 1603–1612, 2007.
[20] D. Gallo, R. Langella, M. Luiso, A. Testa, and N. R. Watson, "A new test procedure to measure power electronic devices' frequency coupling admittance," *IEEE Transactions on Instrumentation and Measurement*, vol. 67, DOI 10.1109/TIM.2018.2819318, no. 10, pp. 2401–2409, 2018.
[21] X. Yue, X. Wang, and F. Blaabjerg, "Review of small-signal modeling methods including frequency-coupling dynamics of power converters," *IEEE Transactions on Power Electronics*, vol. 34, no. 4, pp. 3313–3328, 2018.
[22] J. Man, X. Xie, S. Xu, C. Zou, and C. Yin, "Frequency-coupling impedance model based analysis of a high-frequency resonance incident in an actual mmc-hvdc system," *IEEE Transactions on Power Delivery*, vol. 35, no. 6, pp. 2963–2971, 2020.
[23] S. Zhu, K. Liu, J. Le, K. Ji, Q. Huai, F. Wang, and X. Liao, "Stability assessment of modular multilevel converters based on linear time-periodic theory: Time-domain vs. frequency-domain," *IEEE Transactions on Power Delivery*, pp. 1–1, 2022.
[24] F. Cecati, R. Zhu, M. Langwasser, M. Liserre, and X. Wang, "Scalable state-space model of voltage source converter for low-frequency stability analysis," in *2020 IEEE Energy Conversion Congress and Exposition (ECCE)*, pp. 6144–6149, 2020.
[25] M. Liserre, R. Teodorescu, and F. Blaabjerg, "Multiple harmonics control for three-phase grid converter systems with the use of pi-res current controller in a rotating frame," *IEEE Transactions on power electronics*, vol. 21, no. 3, pp. 836–841, 2006.
[26] H. Yang, H. Just, M. Eggers, and S. Dieckerhoff, "Linear time-periodic theory-based modeling and stability analysis of voltage-source converters," *IEEE Journal of Emerging and Selected Topics in Power Electronics*, vol. 9, no. 3, pp. 3517–3529, 2021.
[27] J. Kwon, X. Wang, F. Blaabjerg, C. L. Bak, V.-S. Sularea, and C. Busca, "Harmonic interaction analysis in a grid-connected converter using harmonic state-space (hss) modeling," *IEEE Transactions on Power Electronics*, vol. 32, no. 9, pp. 6823–6835, 2017.
[28] H. Yang and S. Dieckerhoff, "Truncation order selection method for ltp-theory-based stability analysis of converter dominated power systems," *IEEE Transactions on Power Electronics*, vol. 36, no. 11, pp. 12 168–12 172, 2021.
[29] C. international des grands réseaux électriques. Comité d'études C6 and I. C. on Large Electric Systems, *Benchmark Systems for Network Integration of Renewable and Distributed Energy Resources: Task Force C6.04*, ser. [Brochures thématiques]. CIGRÉ, 2014. [Online]. Available: https://books.google.de/books?id=v3PcoQEACAAJ
[30] N. M. Wereley, "Analysis and control of linear periodically time varying systems," Ph.D. dissertation, Massachusetts Institute of Technology, 1990.
[31] J. K. M. Becker, A. M. Kettner, Y. Zuo, F. Cecati, S. Pugliese, M. Liserre, and M. Paolone, "Modelling of ac/dc interactions of converter-interfaced resources for harmonic power-flow studies in microgrids," *arXiv preprint arXiv:2206.07332*, 2022.
[32] X. Wang, L. Harnefors, and F. Blaabjerg, "Unified impedance model of grid-connected voltage-source converters," *IEEE Transactions on Power Electronics*, vol. 33, no. 2, pp. 1775–1787, 2017.
[33] B. Gao, Y. Wang, and W. Xu, "Modeling voltage source converters for harmonic power flow studies," *IEEE Transactions on Power Delivery*, vol. 36, no. 6, pp. 3426–3437, 2021.
[34] X. Li and H. Lin, "A design method of phase-locked loop for grid-connected converters considering the influence of current loops in weak grid," *IEEE Journal of Emerging and Selected Topics in Power Electronics*, vol. 8, no. 3, pp. 2420–2429, 2019.
[35] H. Gong, X. Wang, and L. Harnefors, "Rethinking current controller design for pll-synchronized vscs in weak grids," *IEEE Transactions on Power Electronics*, vol. 37, no. 2, pp. 1369–1381, 2021.
[36] Z. Zou, G. Buticchi, M. Liserre, A. M. Kettner, and M. Paolone, "Voltage stability analysis using a complete model of grid-connected voltage-source converters," in *2016 IEEE Energy Conversion Congress and Exposition (ECCE)*, pp. 1–8. IEEE, 2016.
[37] P. Kundur, "Power system stability," *Power system stability and control*, vol. 10, 2007.

**Federico Cecati** (S'18-M'22) received the B.Sc and M.Sc. degree in Automatic Control Engineering from the University of L'Aquila, L'Aquila, Italy in 2015 and 2017, respectively. Since 2018 he is a PhD researcher at the Chair of Power Electronics, Kiel University, Kiel, Germany. From September 2020 to February 2021 he was a guest researcher at the Institute of Energy Technology, Aalborg University, Aalborg, Denmark. His research interests include nonlinear modelling, stability analysis, harmonic propagation and control in power electronics-based power systems.

**Johanna Kristin Maria Becker** (S'19) received her B.Sc. degree in Microsystems Engineering from Freiburg University, Germany in 2015 and the M.Sc. degree in Electrical Engineering from the Swiss Federal Institute of Technology of Lausanne (EPFL), Lausanne, Switzerland in 2019. She is currently pursuing a Ph.D. degree at the Distributed Electrical System Laboratory, EPFL, with a focus on robust control and stability assessment of active distribution systems in presence of harmonics.

**Sante Pugliese** (M'18) received the M.Sc. degree in automation engineering and the Ph.D. degree in electrical and information engineering from the Politecnico di Bari, Bari, Italy, in 2013 and 2018, respectively. In 2017, he was a Visiting Scholar with the Chair of Power Electronics, Kiel, Germany, where he is currently a Post-Doctoral Researcher. In 2018-2019, he was Post-doc responsible in the EEMSWEA (0325797A) research project, Medium Voltage Grid Analyzer - Mittel Spannungs Netz Analyse. In 2020 he was Post-doc responsible in the Add-On (0350022B) research project funded by the Bundesministerium für Wirtschaft und Energie. His research interests include power converters and control techniques for distributed power generation systems based on renewable energies.

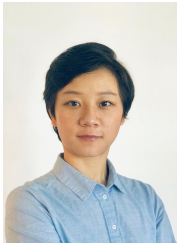

**Yihui Zuo** (M'18) received the B.Sc. and M.Sc. degrees in electrical engineering from North China Electric Power University, Beijing, China, in 2013 and 2016, respectively, and the Ph.D. degree in electrical engineering from the Swiss Federal Institute of Technology (EPFL), Lausanne, Switzerland, in 2021. She is currently a Postdoctoral Fellow with the Distributed Electrical System Laboratory, EPFL. Her research interests focus on power grids with increasing converter-interfaced energy resources, including the development of system-level control for electrical grids and the device control of distributed resources. She has extensive experience in electrical system and control modeling, real-time simulation, and hardware-in-the-loop tests.

**Marco Liserre** (S'00-M'02-SM'07-F'13) received the MSc and PhD degree in Electrical Engineering from the Bari Polytechnic, respectively in 1998 and 2002. He has been Associate Professor at Bari Polytechnic and from 2012 Professor in reliable power electronics at Aalborg University (Denmark). From 2013 he is Full Professor and he holds the Chair of Power Electronics at Kiel University (Germany). He has published 500 technical papers (1/3 of them in international peer-reviewed journals) and a book. These works have received more than 35000 citations. Marco Liserre is listed in ISI Thomson report "The world's most influential scientific minds" from 2014. He has been awarded with an ERC Consolidator Grant for the project "The Highly Efficient And Reliable smart Transformer (HEART), a new Heart for the Electric Distribution System". He is member of IAS, PELS, PES and IES. He has been serving all these societies in different capacities. He has received the IES 2009 Early Career Award, the IES 2011 Anthony J. Hornfeck Service Award, the 2014 Dr. Bimal Bose Energy Systems Award, the 2011 Industrial Electronics Magazine best paper award in 2011 and 2020 and the Third Prize paper award by the Industrial Power Converter Committee at ECCE 2012, 2012, 2017 IEEE PELS Sustainable Energy Systems Technical Achievement Award and the 2018 IEEE-IES Mittelmann Achievement Award.

**Mario Paolone** received the M.Sc. (Hons.) and Ph.D. degrees in electrical engineering from the University of Bologna, Italy, in 1998 and 2002. From 2005 to 2011, he was an Assistant Professor in power systems with the University of Bologna. Since 2011, he has been with the Swiss Federal Institute of Technology, Lausanne, Switzerland, where he is Full Professor and the Chair of the Distributed Electrical Systems Laboratory. His research interests focus on power systems with particular reference to real-time monitoring and operational aspects, power system protections, dynamics and transients. Dr. Paolone's most significant contributions are in the field of PMU-based situational awareness of active distribution networks (ADNs) and in the field of exact, convex and computationally-efficient methods for the optimal planning and operation of ADNs. Dr. Paolone is Fellow of the IEEE and was the founder Editor-in-Chief of the Elsevier journal Sustainable Energy, Grids and Networks.